Atomic and electronic structure of domains walls in a polar metal

Greg Stone, Danilo Puggioni, Shiming Lei, Mingqiang Gu, Ke Wang, Yu Wang, Jianjian Ge, Xue-Zeng Lu, Zhiqiang Mao, James M. Rondinelli, and Venkatraman Gopalan

Phys. Rev. B **99**, 014105 — Published 9 January 2019
DOI: 10.1103/PhysRevB.99.014105

Atomic and Electronic Structure of Domains Walls in a Polar Metal

Greg Stone,[1] Danilo Puggioni,[2] Shiming Lei,[1] Mingqiang Gu,[2] Ke Wang,[3] Yu Wang[4], Jianjian Ge,[4] Xue-Zeng Lu,[2] Zhiqiang Mao,[4,5] James M. Rondinelli,[2,*] Venkatraman Gopalan[1,†]

[1]*Department of Materials Science and Engineering, Department of Physics, and Materials Research Institute, The Pennsylvania State University, University Park, Pennsylvania 16802 USA*
[2]*Department of Materials Science and Engineering, Northwestern University, Evanston, Illinois 602028 USA*
[3]*Materials Characterization Laboratory, Materials Research Institute, The Pennsylvania State University, University Park, Pennsylvania 16802 USA*
[4]*Department of Physics and Engineering Physics, Tulane University, New Orleans, Louisiana 70118, USA*
5Department of Physics, The Pennsylvania State University, State College, PA 16802, USA

Corresponding Authors: [*]jrondinelli@northwestern.edu, [†] vxg8@psu.edu

Abstract

Polar metals counterintuitively bring two well-known phenomena into coexistence, namely, bulk polar displacements, and an electronic Fermi surface giving rise to metallic conduction. However, little is known about the polar domains or domain walls in such materials. Using atomic resolution electron microscopy imaging combined with first principles density functional theory, we show that uncharged head-to-tail walls, and “charged” head-to-head and tail-to-tail walls can exist in the bulk of such crystals of polar metals $Ca_3Ru_2O_7$, where both structural changes at the wall as well as electrostatic considerations define the wall nature. Significant built-in potentials of 30-170 meV are predicted at such walls.

I. INTRODUCTION

Domain walls in polar crystals without inversion symmetry exhibit distinct topologies from symmetry derived polar axis transformations [1–3]. In dielectrics with ferroelectric polarizations, the domains structures can form head-to-tail (H-T), head-to-head (H-H) or tail-to-tail (T-T) geometries [4–7], where the 'head' and 'tail' designations refer to the orientation of the polar displacement vectors of the adjoining domains. Although H-H and T-T domain walls can form in insulating ferroelectrics, they have an associated electrostatic energy cost [5,6,8,9]. Similar domain wall structures should also occur in *band metals*, without inversion symmetry despite an electric polarization being ill-defined, because the domains still exhibit a unique polar axis arising from the atomic structure.

Recent studies of the polar metal $Ca_3Ru_2O_7$ have verified that despite the absence of depolarization fields, polar metals support a rich quasi-two-dimensional polar domain structure that coexists with metallic conductivity [10]. These structures are similar to those found in the isostructural and *insulating* ferroelectrics $(Sr,Ca)_3Ti_2O_7$ [1,11,12] and $Ca_3(Mn,Ti)_2O_7$ [13] where polar displacements arise from anharmonic coupling of oxygen octahedral tilt modes [14–16]. Although one may expect the abundance of free carriers in a polar metal (e.g. $\sim 2.8\times10^{22}$ cm^{-3} in $Ca_3Ru_2O_7$) to dominate the wall properties, there is little understanding of the extent to which charge accumulation or depletion occurs, and is even meaningful in analogous H-H (T-T) domain walls in a metal, and how the electronic structure of the wall differs from that of the bulk domain.

Using aberration-corrected scanning transmission electron microscopy (STEM), we directly image the atomic structure of 90° domain walls in $Ca_3Ru_2O_7$. These images show that the layered nature of $Ca_3Ru_2O_7$ changes the character of the 90° domain walls as it propagates through the crystal.

We find the H-H or T-T domain wall configuration transforms into an H-T wall configuration when intersected by an 180° wall constrained to the rock salt layer, forming a T-junction. Using the experimentally verified wall structures as the input to the density functional theory (DFT) calculations, we show that a significant change occurs in the local density-of-states occurs at these walls, arising from both atomic structural effects (RuO_6 rotations) and the character of the majority charge carrier. The H-H and T-T 90° domain walls in $Ca_3Ru_2O_7$ exhibit distinct electrostatic profiles with a screening length of ~1 nm, which is an order of magnitude larger than that of conventional metals such as copper. Within this screening region, a potential variation of 30 meV to 170 meV occurs, depending on whether the domain wall is H-T, H-H, or T-T. To put the significance of these intrinsic contact potentials occurring in a homogenous material in perspective, we note that a typical silicon-based transistor requires 60 meV/decade to switch between the on and the off states.

II. METHODOLOGIES

A. Single Crystal $Ca_3Ru_2O_7$ Synthesis

Single crystals of $Ca_3Ru_2O_7$ were grown using the floating zone method [17]. Using optical second harmonic generation microscopy, 90° domain walls were identified, which were then prepared into TEM samples using focused ion beam milling. Atomic resolution annular dark field (ADF) STEM images of the domain walls were then collected along the [110] zone axis. From these images, the positions of the Ca and Ru atoms were measured to determine the projection of the polar displacement vectors, $\boldsymbol{v}_P$ and Ca-Ca-Ca angle along [001] θ_P, as defined in Fig. 1(a).

B. Electron Microscopy Details

Scanning transmission electron micrographs of the atomic structure of domain walls in $Ca_3Ru_2O_7$ were obtained using a FEI Titan^3 G2 double aberration-corrected microscope operating at 200 keV and a probe semi-angle of 28.9 mrad. High resolution images of the Ca and Ru atomic positions were capture using an annular dark field (ADF) detect with an inner and outer collection angles of 42 mrad and 244 mrad, respectively. The positions of the Ca and Ru atoms were determine using an in-house developed MATLAB code based on a 2D Gaussian peak fitting scheme. At each location micrograph pairs with the raster scan rotated by 90 degrees were collected for post processing drift correction [18].

C. Computational Details

To calculate the DOS, density functional theory (DFT) calculations were performed within the revised Perdew-Burke Ernzerhof (PEsol) exchange correlation function revised for solids [19,20] as implemented in the Vienna Ab ignition Simulation Package [21]. The projector-augmented wave method [22] was used to treat the core and valence electrons using the following electronic configurations $3s^2 3p^6 4s^2$ (Ca), $5s^2 4d^6$ (Ru), and $2s^2 2p^4$ (O), and a 500 eV plane wave cutoff. A 7 × 1 × 5 Monkhorst-Pack *k*-point mesh [23] and Gaussian smearing (20 meV width) was used for the Brillouin zone (BZ) sampling and integrations. The 1 × 16 × 1 supercells were constructed using the room-temperature lattice constants [24] to model the domain walls. For structure optimization, the atomic positions were relaxed to have forces less than 0.1 meV $Å^{-1}$. Atom-and orbital-resolved DOS are calculated in the nonmagnetic state to mimic the room temperature paramagnetic configuration.

For the calculation of the Seebeck coefficient, we use Boltzmann transport theory [25] within the constant scattering time (τ) approximation as implemented in the BoltzTraP code [26].

These calculations involved a non-self-consistent DFT calculation with a much denser k-point sampling of 24 × 24 × 24 (3,456 k-points in the irreducible BZ; 13,824 k-points in the full BZ), using the bulk equilibrium ground state structure. The Seebeck coefficients S are then calculated independently from τ.

III. RESULTS AND DISCUSSION

A. Crystal and domain wall atomic structure

$Ca_3Ru_2O_7$ adopts a layered structure that belongs to the Ruddlesden-Popper series of compounds ($A_{n+1}B_nO_{3n+1}$) and is comprised of alternating perovskite bilayers of $CaRuO_3$ separated by CaO rock-salt layers, [see Fig. 1(a)]. At room temperature $Ca_3Ru_2O_7$ is metallic and adopts a $Bb2_1m$ symmetry with the polar axis parallel to [010] [24,27]. As recently discussed by Lei et. al. [10], the polar displacements are driven by an anharmonic trilinear coupling of the RuO_6 tilts and rotations about [110] and [001] axes, respectively, resulting in an $a^-a^-c^+$ tilt pattern according to Glazer notation [28]. These lattice modes can be identified using representation theory with the irreducible representations (irreps) of the parent $I4/mmm$ structure: the product of the rotation (X_2^+, $Bbcm$ symmetry) and tilt (X_3^-, $Bbmm$ symmetry) modes stabilize the polar mode (Γ_5^-, $Fmm2$ symmetry). These symmetries and lattice distortions are present at room temperature where we perform our study.

Figures 1(b)-1(d) show ADF-STEM images collected from H-T, H-H and T-T 90° domain walls. While the H-H and T-T 90° domain walls are readily observed in the ADF-STEM images by the change in direction of $\boldsymbol{v}_P$ as seen in Figures 1(c) and 1(d), no such change in $\boldsymbol{v}_P$ is observed for H-T 90° domain walls due to the crystal orientation. Despite this, H-T 90° domain walls can be identified by the tracking changes in θ_P, which increases from the bulk value of 161° to the maximum value of 173° [see Fig. 1(g)]. We note that at H-H and T-T 90° domain walls, θ_P approaches the paraelectric limit of 180° [see Figs. 1(e) and 1(f)]. Closer inspection of θ_P in Figs. 1(e)-(g) reveals that θ_P oscillates between neighboring perovskite bilayers along [001] at the H-H, T-T, and H-T 90° domain walls. This effect is most pronounced at the H-T and T-T 90° domain walls, while it is somewhat weaker at the H-H 90° walls. These results indicate that the CaO layer disrupts the atomic structure of the 90° wall as it propagates along [001] inside the crystal and affects how the interface dipole transforms across the wall.

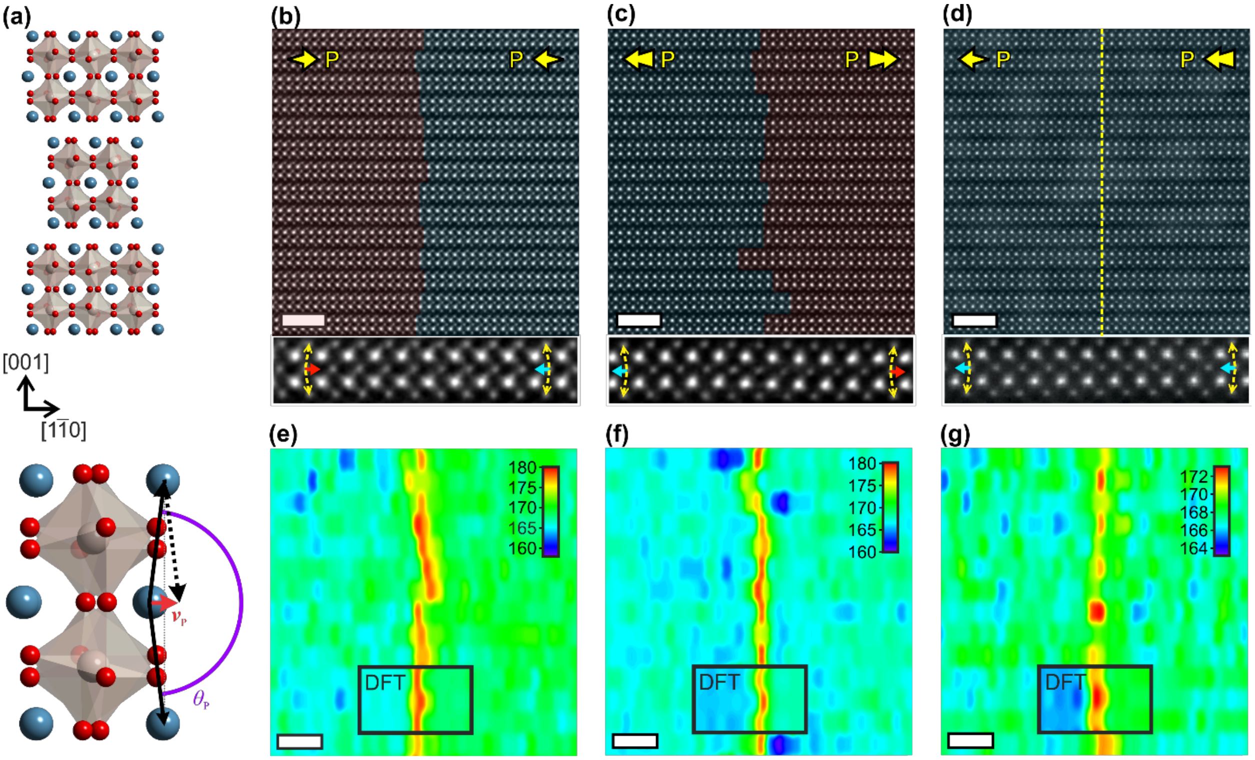

FIG. 1. (a) [110] view of $Ca_3Ru_2O_7$ with a magnified perovskite bilayer showing the Ca displacements (black arrows) which are used to define polar displacement vector $\boldsymbol{v}_P$ and angle θ_P. The Ca, Ru, and O atoms are represented by blue, gray, and red circles, respectively. ADF-STEM images along the [110] zone of (b) H-H, (c) T-T, and (d) H-T 90° domain walls with orientation of $\boldsymbol{v}_P$ indicated by the yellow arrows and the overlaid red and blue features. The yellow dashed line in (d) is a visual guide to the H-T 90° domain wall. Zoomed in regions of the wall show below panels (b)-(d) depict the characteristic polar displacements of the Ca atoms across the domain walls. (e)-(g) Maps of θ_P calculated from the ADF-STEM images of H-H, T-T, and H-T 90° domain walls with DFT derived values overlaid in the black boxes. Scale bars are 2 nm each.

To understand the origins of these structural features at the different types of walls, we performed DFT calculations on two supercell models containing the different 90° domain wall variations. Figure 2(a) shows the first model consists of a single T-T and H-H 90° domain walls, while Figure 2(b) shows the second model possesses two H-T 90° domain walls. Analysis of the relaxed models reveals that the atomic structures of all 90° domain walls are perturbed by the CaO layers. To illustrate this, we present the evolution of the Ru–O–Ru bond angles across the domain walls, which are known to be strongly tied to the electronic and magnetic properties of perovskites [29,30] and are of particular importance in stabilizing the polar structure in metallic $Ca_3Ru_2O_7$ [10]. For the H-T 90° wall, the Ru-O-Ru angle measured along [110] increases from the bulk value of ~150° to values of 156° and ~157° in neighboring perovskite layers [see Fig. 2(c)]. In contrast, the Ru-O-Ru angles for the H-H and T-T 90° domain walls are ~176° in one layer while in the neighboring bilayer they are barely perturbed from the bulk value (150°) to ~152° [see Fig. 2(d)]. The Ru-O-Ru angles along the other two orthogonal directions ([1-10] and [001]) are also perturbed from the bulk value for the H-T, H-H, and T-T 90° walls, but to a lesser degree than the [110] direction [Fig. 2(c)-(d)].

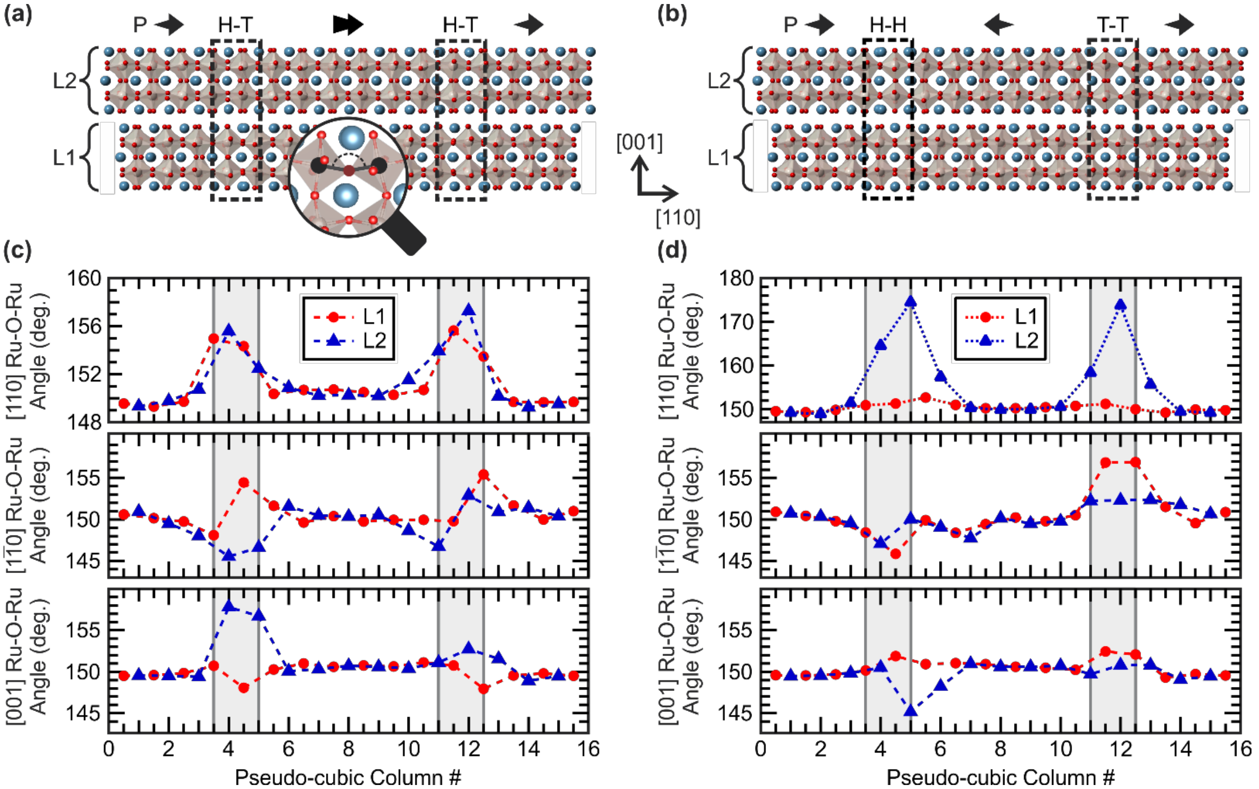

FIG. 2. (a) DFT calculated supercells of (a) head-to-tail and (b) head-to-head (H-H) and tail-to-tail (T-T) 90° domain walls in $Ca_3Ru_2O_7$, with the magnified area in (a) showing the [110] Ru-O-Ru bond angle. The two perovskite bilayers of the supercell structure are labeled L1 and L2. (c-d) Line profiles of the [110], [1-10], and [001] Ru-O-Ru bond angles across H-T, H-H, and T-T domain walls corresponding to the structures in (a) and (b), respectively. Note the strong difference in the [110] Ru-O-Ru bond angles in L1 and L2 for the H-H and T-T 90° domain walls.

Although the anti-phase rotation of the RuO_6 octahedra prevents direct imaging of the Ru-O-Ru bond angles by STEM, it is well established that the displacement amplitude of the A-site atoms in perovskites are linked to the RuO_6 octahedral rotations [31] and consequently the Ru-O-Ru bond angle. To compare the DFT derived wall structures with the STEM data, the position of the Ca atoms in the DFT supercells were used to calculate theoretical values of θ_P across the H-T, H-H, and T-T 90° domain walls. These values show excellent agreement with the STEM derived values in both perovskite bilayers for all three domain walls and also capture the oscillatory behavior of θ_P in neighboring perovskite layers [see insets in Figs. 1(e)-1(g)].

B. Domain Wall Intersections

Close examination of the supercells reveals that the 90° walls alternate between being Ca-site centered and Ru-site centered as it propagates along [001]. This originates from the half pseudocubic unit cell shift along [100] introduced by the CaO rock salt layer between the neighboring perovskite blocks L1 and L2 [see Fig. 2], as seen in the STEM images. Note the effect of being Ca-site centered causes a suppression of the oxygen octahedral rotations and gives rise to the observed difference in behavior of the Ru-O-Ru angle between the L1 and L2 layers [see Fig. 2(d)]. Additional ADF-STEM imaging reveals another interesting structural domain wall feature. At multiple locations within the crystal, we find that T-T (H-H) 90° walls transform into H-T 90° walls upon intersecting a CaO 180° wall [see Fig. 3], which is confined to the CaO rock salt plane. The presence of the H-T 90° wall is confirmed by the corresponding maps of θ_P [see Fig 3(b) and (d)], which show the characteristic oscillating pattern shown in Fig. 1(g). This arrangement of 90° and 180° domain walls is henceforth called a T-junction. The T-junction does not constitute a polar vortex structure and differs from the domain-wall junctions reported by Lee et. al. [12], where two consecutive 90° domain walls introduces a 180° rotation of the polarization in insulating titanates. ADF-STEM images taken along the [100] zone axis (see Fig. 4) verify that the crystal structure does indeed adopt the proposed T-junction structure. It is interesting to note that despite ubiquitous occurrences, the CaO 180° walls were never observed to cross the 90° domain wall. The DFT calculations indicate that the energy difference of the two supercells in Figure 2 is only 4 meV/f.u. in favor of the H-T 90° walls, an energy scale much smaller than room temperature (~25 meV). These results suggest that the elastic penalty paid by the propagation of the CaO 180° wall across the 90° wall is no longer offset by the electrostatic energy penalty associated with H-

H or T-T 90° walls (as would be the case in an insulator), and thus the crystal adopts the T-junction structure.

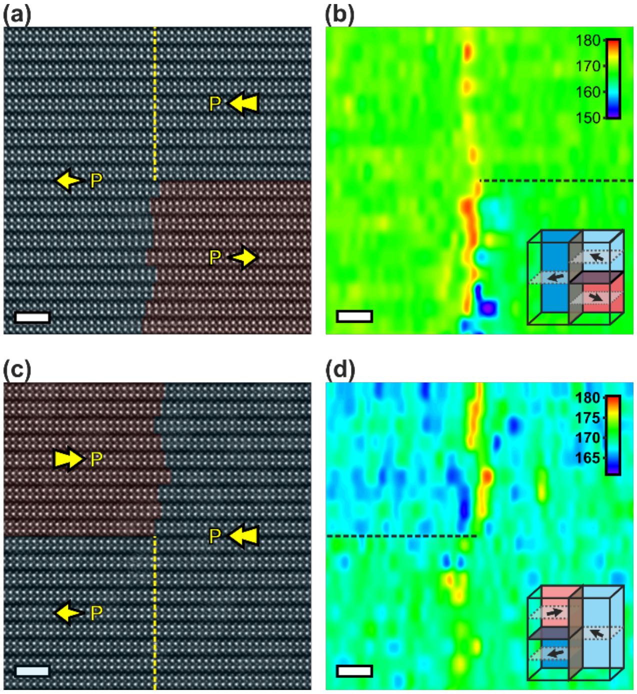

FIG. 2. (a) ADF-STEM image of an intersection of a CaO 180° and 90^{o} domain walls forming a T-junction, which transforms an H-T 90° wall into a T-T 90° wall. The direction of in-plane polarization is indicated by the yellow arrows and overlaid color (blue left, red right). (b) Maps of θ_P showing the characteristic oscillatory pattern for the H-T 90° wall, confirming its presence at the T-junction. Insert, schematic the domain structure at the T-junction. (c) ADF-STEM imaging of a second T-junction at the intersection of an H-T and H-H 90^{o} domain wall and (d) the corresponding θ_P maps of the intersection. Scale bars are 2 nm.

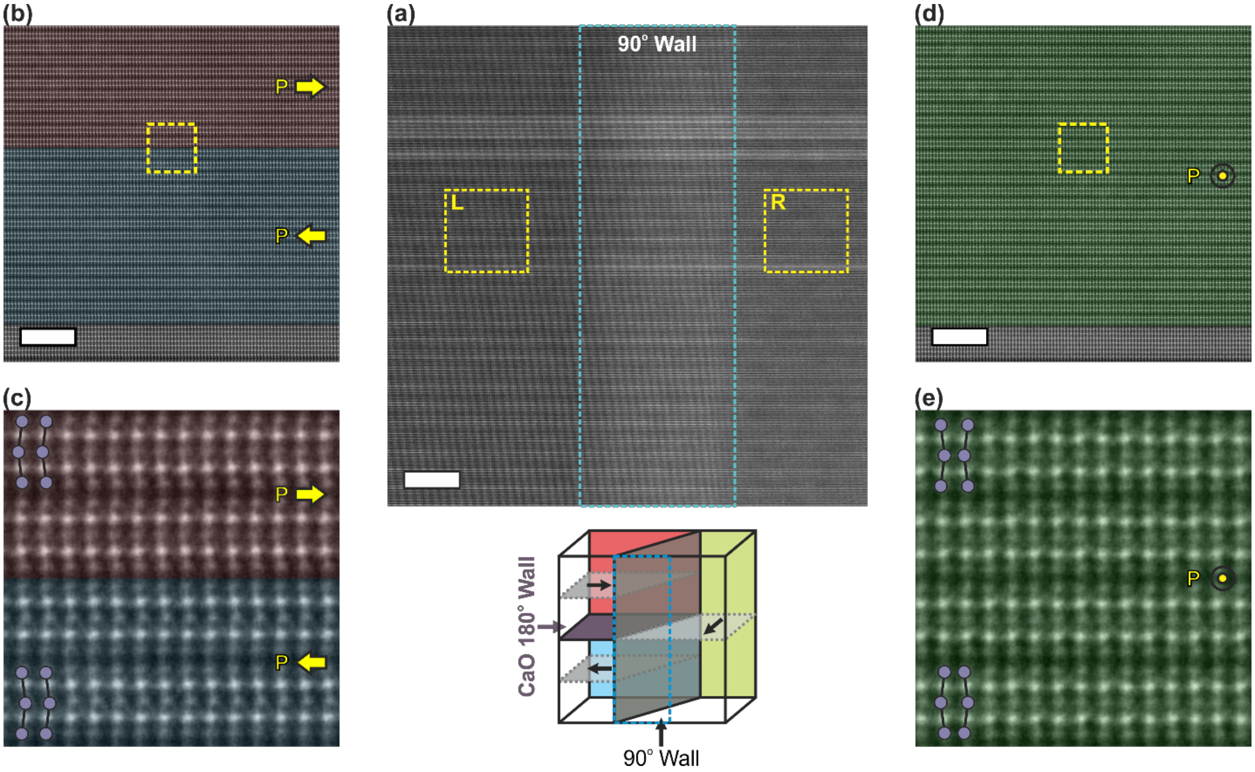

FIG 4. Annular dark field (ADF) STEM image along 90° of a domain wall T-junction in $Ca_3Ru_2O_7$ with an illustration of the observed domain configuration (below). (b) High resolution ADF-STEM image taken from the area left (L) of the 90° domain wall in (a) with the blue and red overlay indicating the polarization orientation. Note, the $n\neq2$ defect layer is used as reference guide. (c) Magnified images of the CaO 180° domain wall taken from the yellow bow in (b) showing a reversal of the Ca polar chevron pattern within the perovskite layer. (d) ADF-STEM images taken from the area to the right of the 90o domain wall. (e) Zoomed in image taken from the yellow box in (d) showing that the polar displacements are no longer in plane confirming the presence of a continuous 90° domain wall across the T-junction.

C. Electronic Structure

Next, we compare the density of states (DOS) at the 90° domain walls to the bulk-like region in the center of the domains. Calculation show that the DOS at the wall is qualitatively similar to the bulk region with the Fermi level (E_F) dominated by the Ru 4d states, consistent with low-spin Ru^{4+}, hybridized with O 2p states [see Fig. 5(a)]; however, upon detailed inspection we find a decrease in the number of states at E_F, $g(E_F)$, for the H-T and H-H 90° walls relative to bulk [see Fig. 5(b)]. In contrast, the number of states at the T-T domain wall is enhanced [see Fig. 5(b)]. Figures 2(c) and 2(d) suggest this change could be attributed to the increase of the Ru-O-Ru bond toward 180° across the 90° domain walls along [110]. This is confirmed by our computational experiment, whereby upon reducing the tilting (X_3^-) and rotation (X_2^+) modes amplitude, the $g(E_F)$ decreases (see Fig. 6). The decrease in states is due to two effects: first, a redistribution of states at E_F via a change in the orbital bandwidth and second, the shift of E_F to higher energy upon reducing the RuO_6 modes (see Fig. 6). The decrease in $g(E_F)$ is expected because all considered 90° domain walls exhibit a smaller tilt of the RuO_6 octahedra [see Figs. 2(c) and 2(d)]. Although this result explains the electronic behavior of the H-T 90° domain wall [see Fig. 5(b)], it cannot account for the differences in $g(E_F)$ at the H-H and T-T 90° domain walls. This finding indicates that additional interactions beyond changes to the local atomic structure are necessary to explain the electronic properties at the H-H and T-T 90° walls.

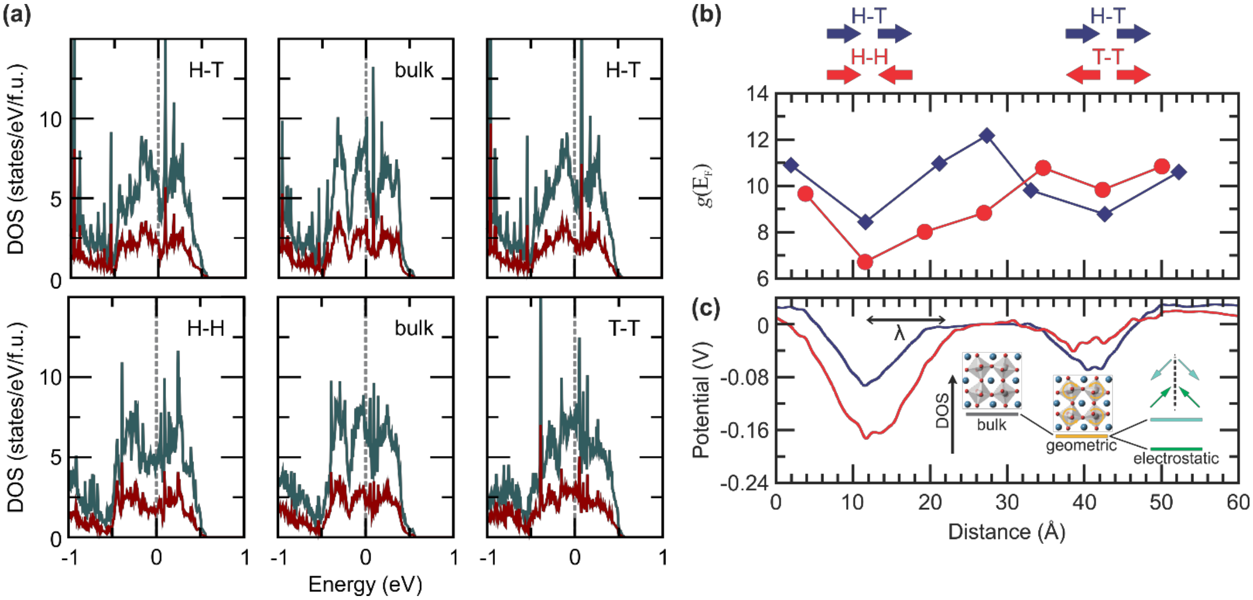

FIG. 5. (a) Projected density of state (DOS) for the H-T and H-H (T-T) 90° domain walls. (b) Number of states at the Fermi level, $g(E_F)$, for the H-T (square) and H-H (T-T) (circle) 90° domain walls. (c) Calculated macroscopic average electrostatic potential with the approximate screening length λ indicated. The inset illustrates the impact of geometric and electrostatic effects on the total DOS in (a) for the different domain walls.

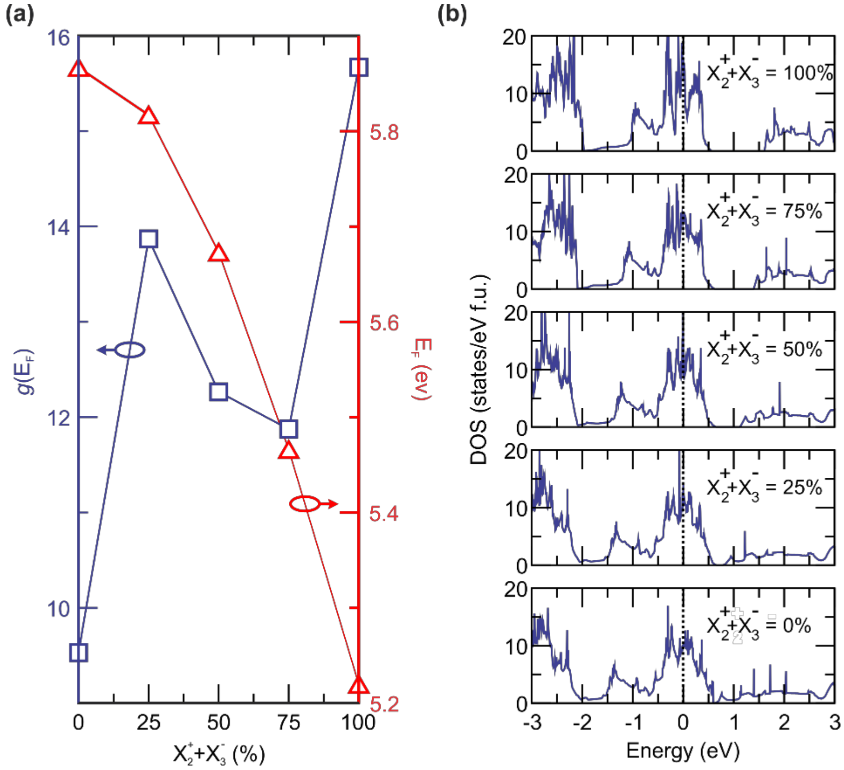

FIG 6. (a) (left) Change in the number of states at E_F, g(E_F) and (right) change in the Fermi level as a function of the RuO$_6$ rotation (X_2^+) and tilt (X_3^-) modes amplitude in bulk Ca$_3$Ru$_2$O$_7$. (b) Total density of states (DOS) for several amplitudes of the X_2^+ and X_3^- modes spanning the ground states crystal structure ($X_2^+ + X_3^- = 100\%$) to no rotation and title ($X_2^+ + X_3^- = 0\%$).

In insulating ferroelectrics, electrostatic interactions at the domain walls arising from bound and free charge are known to greatly influence the electronic properties [6]. However, Ca$_3$Ru$_2$O$_7$ is metallic and therefore long-range electrostatic interactions play only a minor role because they are screened. Despite this expectation, we examined the effect of the polar-axis geometries across adjoining domains on changes to the DOS by calculating the macroscopic average electrostatic potential across the different 90° domain walls. Figure 5(c) shows the macroscopic electrostatic potential changes by approximately 0.1 eV over a distance of 8 Å at both H-T 90° domain walls. This interfacial dipole at the wall is due to the existence of an intrinsic contact potential at a homogenous interface, established by the difference in chemical potentials derived from changes in the Ru-O-Ru bond angles (see Fig. 6). Note that the same result is obtained when vacuum is introduced in the calculation (see Fig. 7). Thus, the potential difference at the H-T 90° domain wall generates a local electric field, with a direction specified by the polarity of the relative Ca and O displacements at the interface. According to the calculations, the local interface dipoles at the 90° domain wall exist over a screening length of $\lambda \approx 10$ Å [see Fig. 5(c)]. This value is large when compared with the Thomas-Fermi screening length for metals that are described as Fermi liquids (e.g. Cu and Zn, $\lambda \approx 0.5$ Å [32]), indicating that $Ca_3Ru_2O_7$ is not a simple band metal.

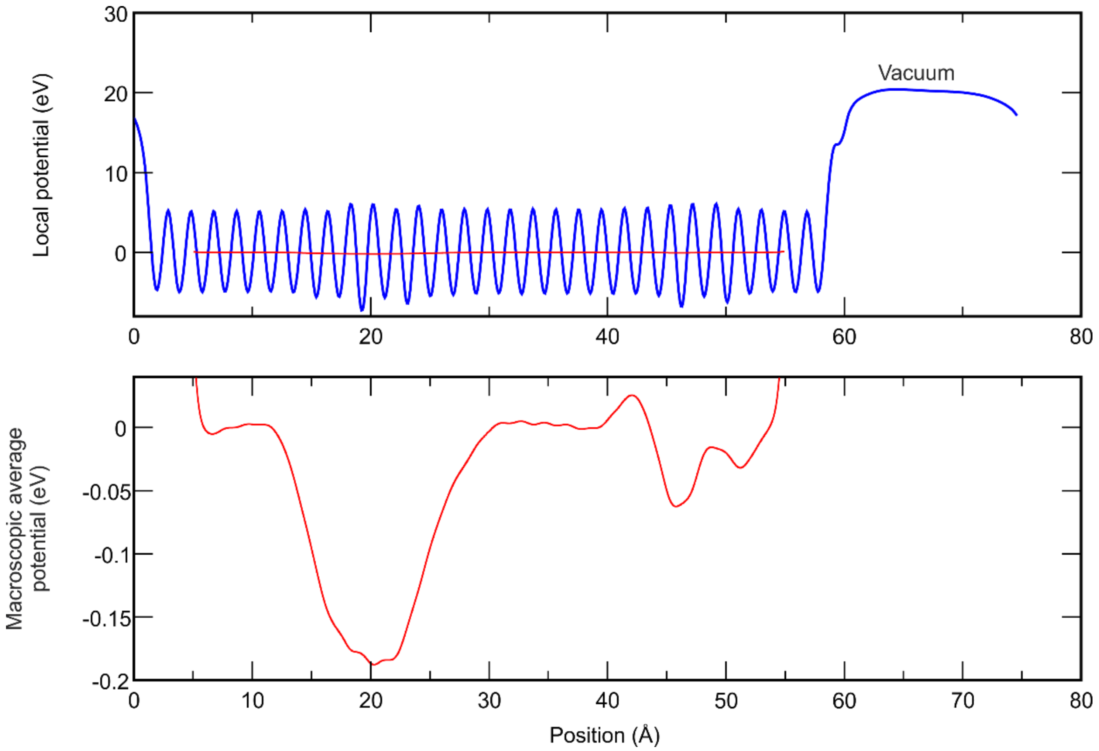

FIG. 7. Calculated local (blue) and macroscopic (red) average potential for the H-H and T-T 90° domain walls with introduction of vacuum in the calculation.

The electrostatic potentials are distinctly different for the H-H and T-T 90° walls [see Fig. 5(c)], despite a similar trend in the Ru-O-Ru bond angles across the wall. In particular, the potential changes at the H-H and T-T 90° domain walls are 0.17 eV and 0.03 eV and occur over large ($\lambda \approx$ 12 Å) and shorter ($\lambda \approx 8$ Å) length scales (nearly a unit cell), respectively. We ascribe these differences to the different polarities at the H-H and T-T 90° domain walls, which in the limit of an insulating dielectric corresponds to positive and negative bound charges, respectively. Our thermopower calculations indicate holes are responsible for the metallic conductivity of $Ca_3Ru_2O_7$ which are only able to compensate the T-T 90° domain wall. For this reason, we find distinctly different electrostatic profiles across what naively should be similar H-H and T-T 90° walls. The analogy to a degenerately doped semiconductor indicates that the H-H 90° wall region would remain depleted of carriers, whereas they accumulate in the T-T 90º wall region. When combined with the geometric effects, these results explain the observed differences in the potential drop and DOS for the different domain walls [see Fig. 5(c)]. Remarkably, this behavior is consistent with what one would find at the domain walls in insulating ferroelectrics, albeit occurring in a high-carrier density metal.

V. CONCLUSIONS

In conclusion, we show that the electronic structure of domain walls in polar metals is influenced both by structural distortions of the lattice and the electrostatic boundary conditions across the wall, resulting in a potential at the wall of tens of meV over ~8-12 Å. A recent study has shown that strain can move these ferroelastic 90° walls in polar metals [10]; therefore, we surmise that such mobile walls at homogeneous interfaces in a metal with a significant built-in potential could potentially be of use as a variable work function gate material and in interface-space charge mediated devices, such as memristors. The work can also help lay the foundation for understanding the critical role of domain walls in the emerging field of non-centrosymmetric metals with non-trivial band topologies [33,34].

ACKNOWLEDGEMENTS

G. S., S. L., and X.-Z.L. were supported by the National Science Foundation (NSF) through the Pennsylvania State University MRSEC under award number DMR-1420620. D.P. and J.M.R. acknowledge the Army Research Office (ARO) under Grant No. W911NF-15-1-0017 for financial support. M.G. was supported by the U.S. Department of Energy (DOE) under Grant No. DE-SC0012375. The crystal growth and characterization at Tulane is supported by the U.S. Department of Energy under EPSCoR Grant No. DE-SC0012432 with additional support from the Louisiana Board of Regents. Calculations were performed using the Extreme Science and Engineering Discovery Environment (XSEDE) and the Department of Defense (DOD) Supercomputing Resource Centers supported by the High-Performance Computing and Modernization Program of the DOD. Electron Microscopy was performed at the Materials Characterization Laboratory (MCL) at the Pennsylvania State University.

References

[1] F.-T. Huang, F. Xue, B. Gao, L. H. Wang, X. Luo, W. Cai, X.-Z. Lu, J. M. Rondinelli, L. Q. Chen, and S.-W. Cheong, Nat. Commun. **7**, 11602 (2016).

[2] W. Wu, Y. Horibe, N. Lee, S.-W. Cheong, and J. R. Guest, Phys. Rev. Lett. **108**, 077203 (2012).

[3] L. Tian, Y. Wang, B. Ge, X. Zhang, and Z. Zhang, Appl. Phys. Lett. **106**, 112903 (2015).

[4] P. R. Potnis, N. T. Tsou, and J. E. Huber, Materials (Basel). **4**, 417 (2010).

[5] P. S. Bednyakov, T. Sluka, A. K. Tagantsev, D. Damjanovic, and N. Setter, Sci. Rep. **5**, 11 (2015).

[6] D. Meier, J. Seidel, A. Cano, K. Delaney, Y. Kumagai, M. Mostovoy, N. A. Spaldin, R. Ramesh, and M. Fiebig, Nat. Mater. **11**, 284 (2012).

[7] M. Y. Gureev, A. K. Tagantsev, and N. Setter, Phys. Rev. B **83**, 184104 (2011).

[8] T. Rojac, A. Bencan, G. Drazic, N. Sakamoto, H. Ursic, B. Jancar, G. Tavcar, M. Makarovic, J. Walker, B. Malic, and D. Damjanovic, Nat. Mater. **16**, 322 (2017).

[9] J. Seidel, L. W. Martin, Q. He, Q. Zhan, Y.-H. H. Chu, A. Rother, M. E. Hawkridge, P. Maksymovych, P. Yu, M. Gajek, N. Balke, S. V. Kalinin, S. Gemming, F. Wang, G. Catalan, J. F. Scott, N. A. Spaldin, J. Orenstein, and R. Ramesh, Nat. Mater. **8**, 229 (2009).

[10] S. Lei, M. Gu, D. Puggioni, G. Stone, J. Peng, J. Ge, Y. Wang, B. Wang, Y. Yuan, K. Wang, Z. Mao, J. M. Rondinelli, and V. Gopalan, Nano Lett. **18**, 3088 (2018).

[11] Y. S. Oh, X. Luo, F. T. Huang, Y. Wang, and S. W. Cheong, Nat. Mater. **14**, 407 (2015).

[12] M. H. Lee, C.-P. Chang, F.-T. Huang, G. Y. Guo, B. Gao, C. H. Chen, S.-W. Cheong, and M.-W. Chu, Phys. Rev. Lett. **119**, 157601 (2017).

[13] B. Gao, F.-T. Huang, Y. Wang, J.-W. Kim, L. Wang, S.-J. Lim, and S.-W. Cheong, Appl.

Phys. Lett. **110**, 222906 (2017).

[14] N. A. Benedek and C. J. Fennie, Phys. Rev. Lett. **106**, 107204 (2011).

[15] N. A. Benedek, A. T. Mulder, and C. J. Fennie, J. Solid State Chem. **195**, 11 (2012).

[16] N. A. Benedek, J. M. Rondinelli, H. Djani, P. Ghosez, and P. Lightfoot, Dalt. Trans. **44**, 10543 (2015).

[17] Y. Yoshida, I. Nagai, S.-I. Ikeda, N. Shirakawa, M. Kosaka, and N. Môri, Phys. Rev. B **69**, 220411 (2004).

[18] C. Ophus, J. Ciston, and C. T. Nelson, Ultramicroscopy **162**, 1 (2016).

[19] J. P. Perdew, A. Ruzsinszky, G. I. Csonka, O. A. Vydrov, G. E. Scuseria, L. A. Constantin, X. Zhou, and K. Burke, Phys. Rev. Lett. **100**, 136406 (2008).

[20] G. Kresse and J. Furthmüller, Phys. Rev. B **54**, 11169 (1996).

[21] G. Kresse and D. Joubert, Phys. Rev. B **59**, 1758 (1999).

[22] P. E. Blöchl, Phys. Rev. B **50**, 17953 (1994).

[23] H. J. Monkhorst and J. D. Pack, Phys. Rev. B **13**, 5188 (1976).

[24] Y. Yoshida, S.-I. Ikeda, H. Matsuhata, N. Shirakawa, C. H. Lee, and S. Katano, Phys. Rev. B **72**, 054412 (2005).

[25] N. W. Ashcroft and D. N. Mermin, *Solid State Physics* (Thomson Learning, Inc., 1976).

[26] G. K. H. Madsen and D. J. Singh, Comput. Phys. Commun. **175**, 67 (2006).

[27] G. Cao, S. McCall, J. E. Crow, and R. P. Guertin, Phys. Rev. Lett. **78**, 1751 (1997).

[28] A. M. Glazer, Acta Crystallogr. Sect. B Struct. Crystallogr. Cryst. Chem. **28**, 3384 (1972).

[29] J. W. Freeland, M. Van Veenendaal, and J. Chakhalian, J. Electron Spectros. Relat. Phenomena **208**, 56 (2016).

[30] G. Catalan, Phase Transitions **81**, 729 (2008).

[31] J. M. Rondinelli, S. J. May, and J. W. Freeland, MRS Bull. **37**, 261 (2012).

[32] S. Kowalczyk, R. Pollak, F. McFeely, L. Ley, and D. Shirley, Phys. Rev. B **8**, 2387 (1973).

[33] B. Yan and C. Felser, Annu. Rev. Condens. Matter Phys. **8**, 337 (2017).

[34] X. L. Qi and S. C. Zhang, Rev. Mod. Phys. **83**, (2011).